A&A 574, A21 (2015)
DOI: 10.1051/0004-6361/201424530

Astronomy & Astrophysics

Isolated elliptical galaxies and their globular cluster systems

II. NGC 7796 – globular clusters, dynamics, companion⋆,⋆⋆

T. Richtler[1,4], R. Salinas[2], R. R. Lane[1], M. Hilker[4], and M. Schirmer[3]

[1] Departamento de Astronomía, Universidad de Concepción, Concepción, Chile
e-mail: tom@astro-udec.cl
[2] Department of Physics and Astronomy, Michigan State University, 567 Wilson Road, MI 48824 East Lansing, USA
[3] Gemini Observatory, Casilla 603, La Serena, Chile
[4] European Southern Observatory, Karl-Schwarzschild-Str. 2, 85748 Garching, Germany

Received 4 July 2014 / Accepted 16 November 2014

ABSTRACT

Context. Rich globular cluster systems, particularly the metal-poor part of them, are thought to be the visible manifestations of long-term accretion processes. The invisible part is the dark matter halo, which may show some correspondence to the globular cluster system. It is therefore interesting to investigate the globular cluster systems of isolated elliptical galaxies, which supposedly have not experienced extended accretion.
Aims. We investigate the globular cluster system of the isolated elliptical NGC 7796, present new photometry of the galaxy, and use published kinematical data to constrain the dark matter content.
Methods. Deep images in *B* and *R*, obtained with the VIsible MultiObject Spectrograph (VIMOS) at the VLT, form the data base. We performed photometry with DAOPHOT and constructed a spherical photometric model. We present isotropic and anisotropic Jeans-models and give a morphological description of the companion dwarf galaxy.
Results. The globular cluster system has about 2000 members, so it is not as rich as those of giant ellipticals in galaxy clusters with a comparable stellar mass, but richer than many cluster systems of other isolated ellipticals. The colour distribution of globular clusters is bimodal, which does not necessarily mean a metallicity bimodality. The kinematic literature data are somewhat inconclusive. The velocity dispersion in the inner parts can be reproduced without dark matter under isotropy. Radially anisotropic models need a low stellar mass-to-light ratio, which would contrast with the old age of the galaxy. A MONDian model is supported by X-ray analysis and previous dynamical modelling, but better data are necessary for a confirmation. The dwarf companion galaxy NGC 7796-1 exhibits tidal tails, multiple nuclei, and very boxy isophotes.
Conclusions. NGC 7796 is an old, massive isolated elliptical galaxy with no indications of later major star formation events as seen frequently in other isolated ellipticals. Its relatively rich globular cluster system shows that isolation does not always mean a poor cluster system. The properties of the dwarf companion might indicate a dwarf-dwarf merger.

Key words. galaxies: elliptical and lenticular, cD – galaxies: individual: NGC 7796 – galaxies: kinematics and dynamics – galaxies: star clusters: general – galaxies: stellar content

1. Introduction

The majority of elliptical galaxies are found in clusters and groups, while relatively few are found in isolation. In spite of their scarcity, isolated galaxies are plausibly important test objects for scenarios of galactic formation, given the relevance of the environment. Massive elliptical galaxies assembled a significant part of their masses and sizes through minor mergers during the past 10 Gyr (van Dokkum et al. 2010). Galaxies in dense environments are therefore expected to experience other modes of growth than galaxies in low density regions. The early catalogues of isolated galaxies (Karachentseva 1973; Karachentseva et al. 1997; Turner & Gott 1976), which used angular distances from photographic plates as isolation criteria, only contain 10% that show an early-type morphology. More modern morphological analyses based on SDSS-images identify about 3% of elliptical galaxies among the sample common to Karachentseva's catalogue and the SDSS (Hernández-Toledo et al. 2008), the majority showing some kind of distortion like diffuse haloes, shells, and dust lanes. However, in another sample of nine extremely isolated galaxies, only two obvious merger remnants have been found (Marcum et al. 2004).

Population studies of isolated ellipticals (IEs) have been performed by Kuntschner et al. (2002) and Collobert et al. (2006). They find typically younger ages and wider age spreads, as predicted from models of galaxy formation in a standard cosmological cold dark matter (CDM) scenario (Kauffmann 1996; Niemi et al. 2010). Photometric properties of IEs have been investigated by Reda et al. (2004), who found that under closer scrutiny half of their galaxy sample show morphological peculiarities. Smith et al. (2004) presents an independent sample of IEs and studied their companions. The work by Hau & Forbes (2006) is an important source for data regarding the central kinematics of IEs.

⋆ Based on observations taken at the European Southern Observatory, Cerro Paranal, Chile, under the programme 089.B-0457. Partly based on observations taken at the Las Campanas Observatory and the Gemini observatory (GS-2011B-Q83).

⋆⋆ The catalogue of the photometry is only available at the CDS via anonymous ftp to cdsarc.u-strasbg.fr (130.79.128.5) or via http://cdsarc.u-strasbg.fr/viz-bin/qcat?J/A+A/574/A21

Many present morphologies with the signature of mergers that are highly visible (see also Tal et al. 2009; Lane et al. 2013). Others, even without obvious visible disturbances, show intermediate ages through their dynamics. Given the structural parameters, the central velocity dispersion is closely related to the stellar mass-to-light ratio (M/L), which in turn can indicate the age. An example is NGC 7507 with an M/L value of 3.1 in the R-band, which is too low for an old population (Salinas et al. 2012).

A classical attribute of giant elliptical galaxies in clusters is their rich globular cluster systems (GCSs). There is now strong evidence that the majority of metal-poor clusters (which dominate the GCSs of giant ellipticals) have been accreted through the accretion of dwarf galaxies (see Richtler 2013, for a recent review). One would, therefore, expect that isolated ellipticals have poorer GCSs, and for most of the investigated galaxies this is indeed the case (Spitler et al. 2008; Lane et al. 2013; Caso et al. 2013). However, the galaxy sample of Cho et al. (2012) suggests that the role of the environment is minor in comparison to the host galaxy mass as parameter.

Within the ΛCDM framework, it is reasonable to also expect a connection of a hierarchically built-up dark matter halo with an accreted GCS. For example, IEs should have less dark matter than giant ellipticals in clusters (Niemi et al. 2010).

Little is known about the dark matter content of isolated ellipticals, and what is known is sometimes not reliable. For example, NGC 7507 had the reputation of a dark matter dominated galaxy (Kronawitter et al. 2000), but a closer look revealed that it is possible to construct models without dark matter (Salinas et al. 2012).

So it is of great interest to investigate more IEs to find out whether NGC 7507 is just a weird outlier or whether it represents a systematic still to be discovered. Studies centered on dark matter halos of isolated ellipticals use in their majority X-ray data (Buote et al. 2002; Mulchaey & Zabludoff 1999; O'Sullivan et al. 2007; Memola et al. 2011; Milgrom 2012). While the existence of dark matter halos (or, depending on the perspective, effects of modified gravity) are generally not questioned, the exact amount of dark matter in a given galaxy can be uncertain. However, NGC 7507 is not unique. Using the kinematics of planetary nebulae in NGC 4697, Méndez et al. (2009) found a declining projected velocity dispersion, which leaves not much room for dark matter.

In this paper, we focus on NGC 7796, investigating its GCS, and developing a simple dynamical model on the basis of literature data. NGC 7796 has been selected from the catalogue of IEs by Reda et al. (2004). To our knowledge, this is the first publication exclusively devoted to this galaxy. NGC 7796 has no immediate neighbours with known radial velocities, but, as we show in this paper, has a dwarf companion with a tidal tail. Table 1 lists the basic data.

The NED[1] lists seven dwarf galaxies with similar redshifts within a projected distance of 400–600 kpc. Spectroscopy of the central regions indicates that the galaxy is old and metal-rich (Bertin et al. 1994; Thomas et al. 2005; Milone et al. 2007; Beuing et al. 2002). NGC 7796 is among the galaxies dynamically modelled by Magorrian & Ballantyne (2001; based on the Bertin et al. 1994 data), who found evidence for a dark halo, and it has a counterrotating core (Bettoni et al. 2001).

We adopt a distance of 50 Mpc, corresponding to 242.4 pc/arcsec. This paper is the second in a series on isolated ellipticals. Paper I is Lane et al. (2013).

[1] NASA Extragalactic Database: http://ned.ipac.caltech.edu/

Table 1. Basic and derived parameters for NGC 7796.

Parameter	Value	Ref.
Right ascension (2000)	23h 58m 59.8s	NED
Declination (2000)	–55d 27m 30s	NED
Rad. velocity	3364 km s^{-1}	NED
Distance	49.9 Mpc	Tonry et al. (2001)
Scale	1″ = 242.4 pc	
$R_{\rm eff}$	21″	RC3
$R_{\rm eff}$	31.8″	Present paper (<300″)
V_T	11.49	NED
A_V	0.03	NED
$B-V$	1.00	Poulain (1988)
$U-B$	0.70	″
$V-R$	0.56	″

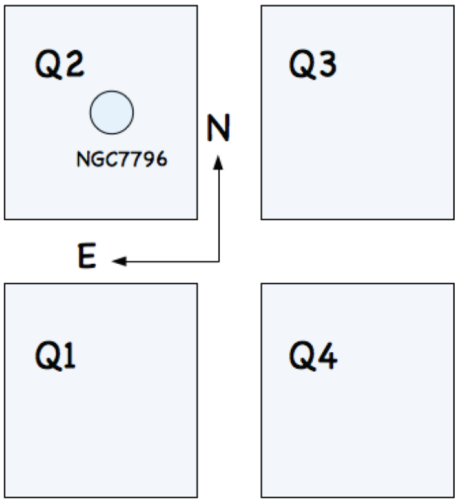

Fig. 1. Arrangements of the VIMOS quadrants for a position angle of 90°. The chips have sizes of 7′ × 8′. The chip gaps have a width of 2′. The VIMOS field in the distance of NGC 7796 therefore covers 235 × 209 kpc^2. NGC 7796 is centered on quadrant 2.

2. Observations and reductions

2.1. Very Large Telescope/VIMOS

The observations were taken using the ESO VLT/UT3 (Melipal)/VIsible MultiObject Spectrograph (VIMOS) on the nights of July 22 and 24, 2012. VIMOS has a nominal field of view of 4 × 7′ × 8′ separated by 2′ gaps, with a pixel scale of 0.205″ (see Fig. 1). Images were obtained through Bessell B and R filters, with total exposure times of 8 × 830 and 16 × 430 s, respectively.

Image reduction was done with the reduction recipes within the ESO VIMOS pipeline (v.2.6.14) operated through GASGANO (v.2.4.3). Master bias and flat frames were produced from calibrations taken on the same nights as the science observations. Bias removal, flat fielding and median combination for each VIMOS quadrant were subsequently done with the recipe *vmimobsjitter*. The final combined images have seeing values of 0.7″ and 0.74″ in B and R, respectively, averaged over the four quadrants.

2.2. Magellan/Baade/IMACS

The idea behind our IMACS observations was to image a large field with deep photometry and to search for tidal features

Table 2. Transformation equation coefficients for Eqs. (1) and (2) for the different quadrants.

Quadrant	Zero-point		Color term		N_{stars}	rms	
	B	*R*	*B*	*R*		*B*	*R*
Q1	27.477 ± 0.012	27.371 ± 0.029	−0.015 ± 0.011	0.030 ± 0.006	24	0.034	0.023
Q2	27.440 ± 0.013	27.361 ± 0.008	0.010 ± 0.010	0.008 ± 0.006	29	0.026	0.022
Q3	27.421 ± 0.028	27.197 ± 0.017	0.041 ± 0.026	−0.025 ± 0.014	24	0.068	0.035
Q4	27.560 ± 0.011	27.326 ± 0.016	0.011 ± 0.017	−0.018 ± 0.014	20	0.042	0.038

on a larger scale than possible with VIMOS (see Sect. 5.3). We observed NGC 7796 with the focal reducer IMACS at the 6.5 m *Magellan/Baade* telecope at the Carnegie observatory at Las Campanas, Chile, on the night of August 8, 2013. In the f/2 mode, IMACS provides a circular field of 27′ with a pixel scale of 0.2″/pixel. Eleven 600 s exposures were taken in Bessell V2 with two overlapping pointings. The seeing on the final image is 0.76″.

The removal of instrumental signatures, astrometric alignment, and co-addition of the 11 individual images was carried out using the THELI-data reduction pipeline (Erben et al. 2005; Schirmer 2013).

3. Photometry with the VIMOS data

The photometry was performed on images with the galaxy light removed. To model the galaxy light, we applied a quadratic median-filter with a side-length of 15 pixels. Given the FWHM of the point-spread-function (PSF) of 3.5 pixels, the median size is large enough to not modify point-sources.

For the photometry of globular cluster (GC) candidates, we used DAOPHOT within the MIDAS environment. We chose the parameters of the finding routine to find about 10 000 objects in each quadrant. The actual number of remaining sources at faint magnitudes is then determined by the PSF-photometry, which discards many objects, and the matching between the *B*- and the *R*-filter. Typically 15 PSF-stars in each quadrant were found. The *allstar*-routine selected about 2/3 of all sources. Matching the lists in the *B* and *R* filters, many of the faintest objects did not find partners, which had been searched for with a maximum displacement of 5 pixels. Finally, the numbers of objects with both *B* and *R* photometry were the following: Q1: 5222; Q2:5742; Q3:5299; Q4:6717.

3.1. Photometric calibration

The photometry was calibrated into the standard Johnson *B* and *R* with observations of the Landolt (1992) field PG1323 which also includes several secondary Stetson standards[2].

The transformation equations to the standard system used were

$$B_{\rm obs} = B_{\rm std} + Z_B + K_B(X-1) + b_B(B-R)_{\rm std} \quad (1)$$

$$R_{\rm obs} = R_{\rm std} + Z_R + K_R(X-1) + b_R(B-R)_{\rm std} \quad (2)$$

where *X* is the airmass of the observation. Coefficients were obtained using IRAF/PHOTCAL. The observations have been done in photometric conditions, but the airmass coverage was too small for an independent calibration, so the extinction coefficients were fixed to values $K_B = 0.242$ and $K_R = 0.08$ taken from the ESO webpages. The rest of the coefficients for each quadrant can be seen in Table 2.

[2] http://www3.cadc-ccda.hia-iha.nrc-cnrc.gc.ca/community/STETSON/standards/

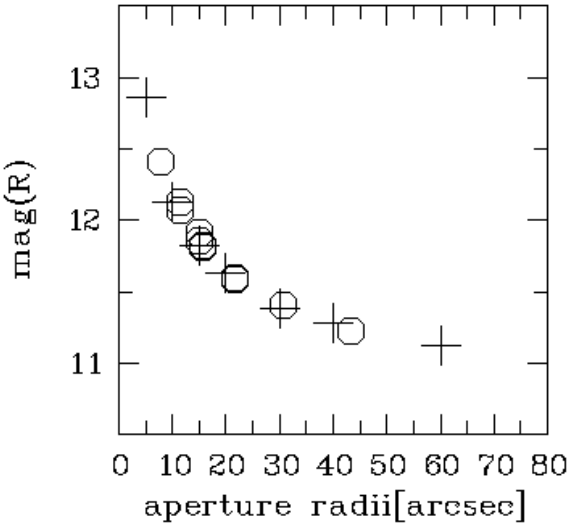

Fig. 2. Check of our *R*-band calibration. Polygons: aperture photometry from Prugniel & Heraudeau (1998). Crosses: radii of simulated apertures from our model profile.

3.2. Comparison with aperture photometry

Support for the quality of our calibration comes from the comparison with aperture photometry. We use our spherical light model (described in Sect. 5.1) to simulate aperture photometry by Prugniel & Heraudeau (1998). This is shown in Fig. 2, where the simulated apertures are compared with measurements. The agreement is excellent, to within 0.02 mag.

3.3. Point source selection

We did not apply very strict selection criteria to maintain the depth of the photometry. Figure 3 shows as an example the distribution of *chi* and *sharp*-values for Quadrant 4 in the *R*-band. The DAOPHOT *chi*-parameter measures the chi-square deviation, when fitting the PSF to given objects, and the *sharp*- parameter measures kurtosis-like deviations (see the DAOPHOT users manual for more information). Ideally, both parameters should be zero for stars and ideal PSFs. The two sequences for stellar-like objects and galaxies are discernible. For magnitudes fainter than about $R = 24$ mag, stellar-like and extended objects partly merge regarding their parameters and a strong restriction only

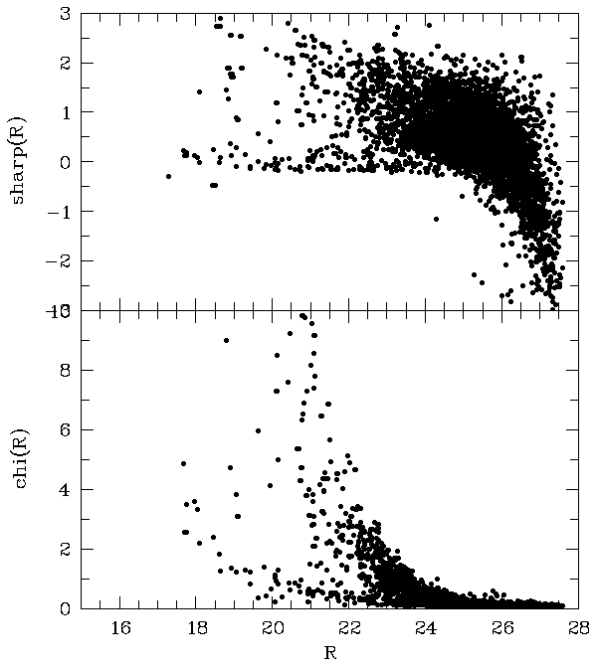

Fig. 3. Distribution of the DAOPHOT *chi* and *sharp* parameters is shown for Quadrant 4 in the *R*-band. The different sequences of stellar-like objects and galaxies are easily distinguished. We apply the selection *chi* less than 1 and *sharp* between −0.5 and 1.

results in a pronounced incompleteness at faint magnitudes. We therefore apply only a mild selection using the *R*-band photometry. The selection is: *chi* less than 1 and *sharp* between −0.5 and 1. This leaves 3728, 3171, 3351, and 4548 objects in Q1–Q4, respectively. The photometry in Q4 clearly is the deepest (see Fig. 4).

4. The globular cluster system

4.1. Colour-magnitude diagram

The arrangement of the VIMOS chips are shown in Fig. 1. The projected distance of the frame border of Q3 is about 75 kpc away from the centre of NGC 7796. The parts of quadrants 3 and 1, which lie nearest to NGC 7796, may therefore contain still some GCs. The foreground reddening towards NGC 7796 is small ($E[B-R] = 0.015$ mag according to Schlegel et al. 1998) and we neglect it. The upper panels in Fig. 4 show the colour-magnitude diagrams (CMDs) in the various quadrants without applying any selections. Quadrant 2 contains NGC 7796 and its entire field is plotted. The GCs is immediately striking. The lower panels show the CMDs with the previously discussed selection for point sources. Moreover, a radius selection is applied for Q2, and the GCS appears even more prominent, and a bimodality is visible without any statistical aid. The vertical dashed lines indicate the theoretical colour of an old GC population for the metallicities [Fe/H] = −2.3 and solar metallicity, using the models of Marigo et al. (2008). The red (metal-rich) limit is precisely defined. This gives weight to the observation that the blue (metal-poor in the case of old clusters) part is more or less empty in the regime of bright clusters.

The vertical sequence of blue clusters seems to be tilted. We do not think that this is a metallicity effect and we return to this point in the discussion.

4.2. Colour distribution

We evaluate the colour distribution in bins of 0.05 mag, using the quadrants Q1, Q3, Q4 as background fields to subtract the background from Quadrant 2. The limiting magnitude was set to 25.5 to avoid the faintest luminosity bins, where the photometry in the region of NGC 7796 is strikingly less complete than in the other quadrants. Figure 5 shows the results, with surface densities (numbers per square arc min) plotted against colour.

The leftmost panel shows the cluster system within 1.5′ (21.8 kpc), where the red clusters slightly dominate. The middle panel depicts the region between 1′ and 2.75′ (14.5 kpc and 40 kpc). The right panel shows the entire cluster system within 2.75′.

The background subtraction leaves a clean colour interval $1.1 < B-R < 1.75$ corresponding to almost the full metallicity spread of old GCs. The vertical dashed lines in Fig. 5 indicate the colour of the models by Marigo et al. (2008) for 11.2 Gyr old clusters and for the metallicities [Fe/H] = −2.3 ($B-R = 0.96$) and [Fe/H] = 0.04 ($B-R = 1.78$). Younger GCs in larger numbers, which are bluer than $B-R = 0.95$, are absent. The relative amplitudes of the blue and the red peaks do not change much with radius, indicating that the respective density profiles are not very different. The inner red peak may be a bit higher than the blue peak, but only marginally, given the uncertainties. At least, it is very different from, for example, Fig. 10 by Dirsch et al. (2003), where the red GC population in NGC 1399 becomes minor at large distances. The shallower profile of the blue GCs, which is quite common in rich GCSs, probably reflects the assembly process by the infall of dwarf galaxies. In Sect. 4.4 we directly compare the number density profiles of blue and red clusters with the galaxy light profile and do not see striking differences.

The widely discussed bimodality (e.g. Richtler 2013), although details are still under debate, has a quite well accepted explanation. We make respective remarks in the discussion.

4.3. Number counts and specific frequency

To estimate the total number of clusters, one should ideally know the luminosity function (LF) down to 1–2 mag below the turnover magnitude (TOM). The absolute TOM in the *R*-filter in *old* GCSs is about −7.9 (Richtler 2003; Rejkuba 2012). We therefore expect the TOM to be around $R = 25.6$, whereas our photometry is already incomplete at brighter magnitudes. One possibility would be to perform experiments with artificial stars to determine completeness factors in dependence on radius and magnitude. This would be a quite complex procedure, because the completeness in the different quadrants probably depends in a complicated way on the matching procedure, and it remains to be shown whether the completeness of artificial stars is the same as for real star images. Moreover, because we can renounce a precise knowledge of the completeness factors, we prefer an easier method.

In Fig. 6, left panel, the surface densities (background subtracted, see Table 3 for the background counts) of GCs in 5 different radius intervals are plotted. It is clear that the completeness factors are quite different. The inner region offers good statistics, but the galaxy light makes the faintest magnitude bins incomplete. The outer bins are more complete, but the number density becomes so low that the uncertainty of the background subtraction becomes dominant. As a compromise between number statistics and completeness, we adopt the LF No. 3 (see caption Fig. 6) (squares) as reference, assuming that it is complete

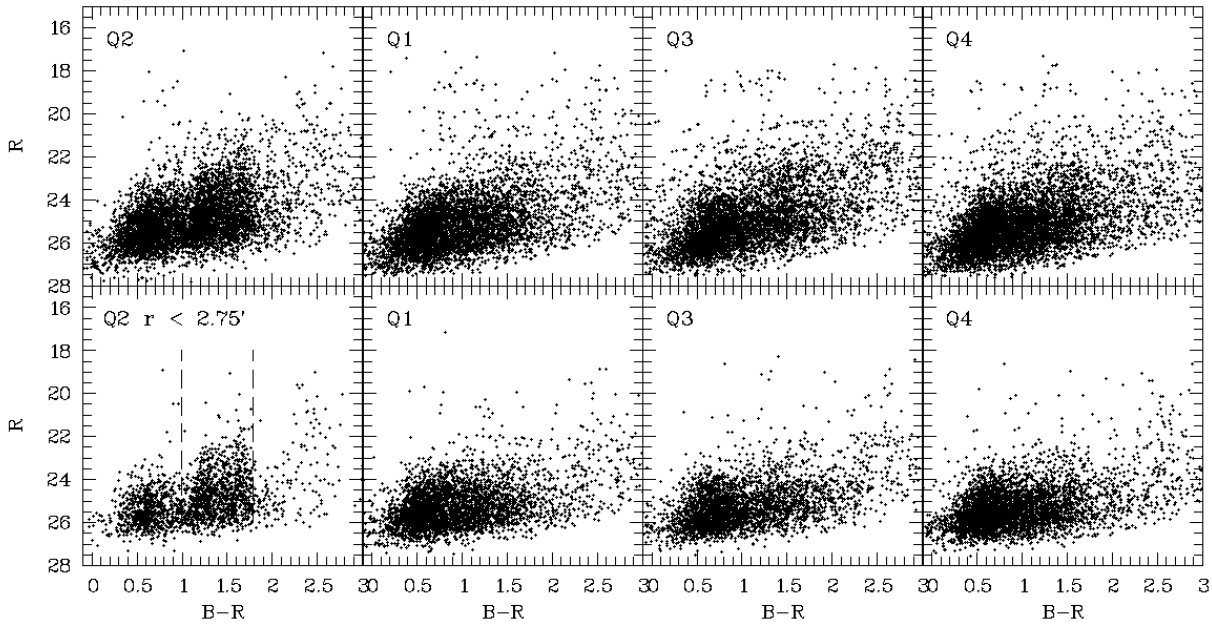

Fig. 4. *Upper panels*: CMDs of the single quadrants without any selection. The *lower row* uses the point source selection as described in the text. Moreover, the Q2-CMD plots only objects with distances less than 2.75′ to the galaxy center. The GCS of NGC 7796 is very prominently seen, including its bimodal colour distribution. Note the sharp borders in colour. The vertical dashed lines mark the metallicities $Z = 0.001$ ([Fe/H] = −2.3) and $Z = 0.04$ ([Fe/H] = +0.3) for GCs of 11.2 Gyr according to Marigo et al. (2008). Some of the brighter objects of the ($R = 22$ mag corresponds to $M_R = -11.5$) must be bright GCs as well.

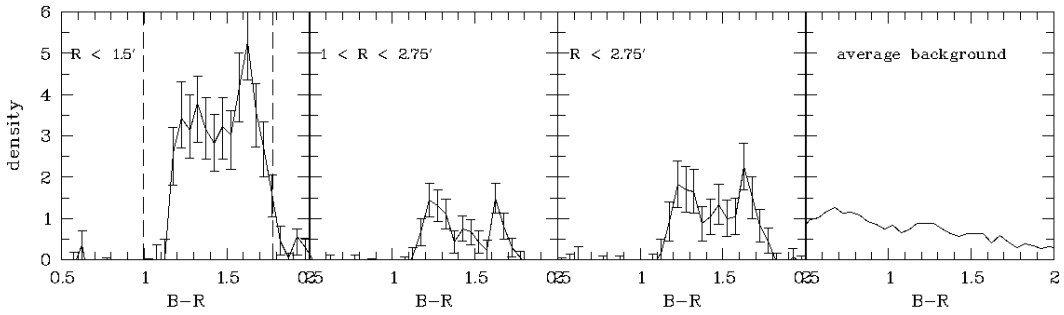

Fig. 5. Surface density of GCs vs. the colour for three different radial bins. The vertical dashed lines in the *left panel* indicate the colour of the models of Marigo et al. (2008) for 11.2 Gyr old clusters and for the metallicities $Z = 0.001$ ([Fe/H] = −2.3; $B - R = 0.99$) and $Z = 0.04$ ([Fe/H] = +0.3; $B - R = 1.78$). The *rightmost panel* is the background. The distinct bimodal appearance remains visible at all radii.

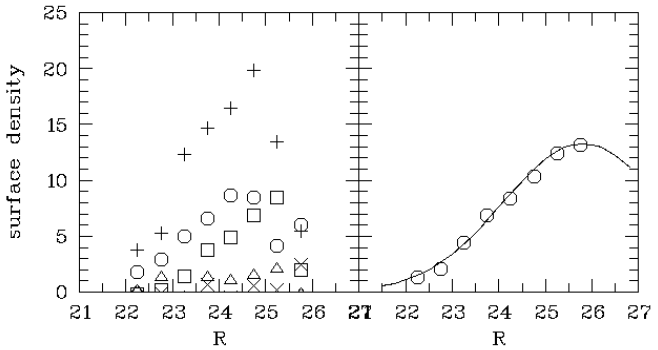

Fig. 6. *Left panel*: LFs of clusters (numbers per square arcmin) for different radius intervals. Under the assumption that the LFs are not radius dependent, we estimate the incompleteness in the two faintest magnitude bins. (1) Plus signs: 0.15′–0.8′; (2) polygons: 0.8′–1.3′; (3) squares: 1.3′–1.8′; (4) triangles: 1.8′–2.3′; (5) crosses: 2.3′–2.8′. *Right panel*: average density after corrections in the radial interval 0.15′–1.8′. A Gaussian with a peak magnitude of $R = 25.8$ and $\sigma_R = 1.7$ is a good fit to the data.

until $R = 25.25$ and that the last bin is the TOM. Therefore, we adjust the last bin by shifting it to the same density of the bin at $R = 25.25$, that means a value of 8.5. We do the same with the two inner LFs. The adopted densities are given in Table 3 in parentheses. The two outer LFs are not longer considered because of their low numbers. The right panel of Fig. 6 shows the total "corrected" densities. The resulting total number of objects brighter than the TOM according to Table 3 within a projected radial annulus of 0.15′–1.8′ (corresponding to 2.2 kpc –26.2 kpc) is then 589 ± 47.

The uncertainties are calculated by assuming Poisson errors for the original count rates. The background has been determined as the average background in the quadrants Q1, Q3, Q4 with the areas 46.23, 41.1, and 47.72 square arcmin, respectively.

If we assume that the number density profile of GCs in NGC 7796 follows the galaxy light (we justify that with Fig. 7), we can use our photometric model to reproduce the inner GC densities and calculate the fraction of clusters, which fall outside this range. We (somewhat arbitrarily, but introducing

Table 3. Background subtracted counts in radial and magnitude bins.

Mag/radius	0.15–0.8 arcmin	0.8–1.3 arcmin	1.3–1.8 arcmin	1.8–2.3 arcmin	2.3–2.75 arcmin	Background
22.25	3.8 ± 1.5	1.8 ± 0.8	0 ± 0.2	0.1 ± 0.3	0	0.36 ± 0.05
22.75	5.2 ± 1.7	3.0 ± 1.0	0.2 ± 0.4	1.3 ± 0.5	0	0.37 ± 0.05
23.25	12.3 ± 2.6	5.0 ± 1.4	1.4 ± 0.7	0 ± 0.3	0	1.07 ± 0.09
23.75	14.7 ± 2.9	6.6 ± 1.6	3.8 ± 1.0	1.3 ± 0.7	0.6	1.32 ± 0.10
24.25	16.4 ± 3.2	8.7 ± 1.9	4.9 ± 1.3	1.0 ± 0.8	0	3.15 ± 0.15
24.75	19.9 ± 3.6	8.5 ± 2.0 (10 ± 2.3)	6.8 ± 1.6	1.5 ± 1.0	0.6	4.87 ± 0.19
25.25	13.5 ± 3.2 (23 ± 5.4)	4.2 ± 1.8 (12 ± 5.1)	8.5 ± 1.8	2.1 ± 1.2	0.2	6.10 ± 0.21
25.75	5.4 ± 2.5 (23 ± 10.6)	6.0 ± 2.0 (12 ± 4.0)	2.0 ± 1.4 (8.5 ± 5.9)	0 ± 1.0	2.4	6.40 ± 0.22
Total	229 ± 26	194 ± 25	166 ± 30	–	–	

Notes. Values are given in units of objects/square arcmin. The total number is the (corrected) density multiplied with the area.

only a small error) cut the GCS at 10 effective radii (77 kpc). The luminosities in the three areas <0.15′, 0.15′–1.8′, 1.8′–5.35′ are 1.96×10^{10} $L_\odot$, 4.93×10^{10} $L_\odot$, and 1.97×10^{10} $L_\odot$, respectively. In proportion to the luminosities, we assign to the inner area 0.4×589 GCs, to the outer area the same number and get 1060 GCs. Since that is the number until the TOM, we double it and get 2120 ± 170 GCs as the grand total, scaling the uncertainty of the counts with the total number. The absolute R-mag in the same area is −22.9. With $V - R = 0.6$, one gets $S_N = 2.5$ for the specific frequency. To estimate the final uncertainty, we allow 10% uncertainty in the distance, which means an uncertainty of 0.22 mag of the absolute magnitude. The squared uncertainties in S_N from the distance and counts are then 0.22 and 0.04, respectively, and the final error is 0.5.

Values of other IEs are lower (e.g. Caso et al. 2013), but intermediate-age and therefore brighter stellar populations contribute significantly to a lower S_N.

The globular cluster luminosity function (GCLF) can serve as a good distance indicator (Richtler 2003; Rejkuba 2012; Villegas et al. 2010) provided that the GCLF reaches beyond the turn-over magnitude (TOM). This is not the case with the present data, but in the right panel of Fig. 6 we show that a Gaussian with $\sigma_R = 1.7$ and a TOM of $R = 25.8$ is a good representation and fits to the adopted distance of 50 Mpc. Since the TOM is barely reached, we cannot say anything about a possible population of younger clusters.

4.4. Number density profile

The density profile of a GCS permits a qualitative assessment of the relation between the GCS and its host galaxy. For example, if the metal-poor population of a GCS has a shallower density profile than its metal-rich counterpart or its host galaxy, as it is normally the case, then it may be interpreted as the effect of infall processes which are responsible for a large part of the GC population.

The number density profile can be simply calculated by using the counts from Table 3. This is shown for magnitudes brighter than $R = 25$ in the left panel of Fig. 7. The solid line is the galaxy luminosity profile with an arbitrary scaling. It is clear that the galaxy profile is a very good representation.

The right panel displays blue (triangles) and red (circles) clusters separately. Considering only the three inner bins, the profile of the blue clusters might be a bit shallower, but the uncertainty prohibits a clear statement. The linear slope for the blue clusters is −1.61 ± 0.6, for the red clusters −1.89 ± 0.3. The best

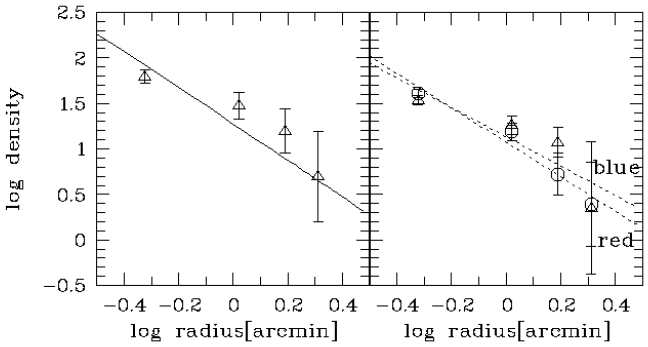

Fig. 7. *Left panel*: density profile (logarithm of numbers per square arcmin) of all GC candidates brighter than $R = 25$ mag. The straight line is the arbitrarily scaled light profile of the galaxy for showing that these profiles are not distinguishable. *Right panel*: the density profiles for red (circles) and blue (triangles) clusters separately. The labels "blue" and "red" indicate the respective linear fits. The blue clusters show a marginally shallower profile, but the uncertainties are too large to draw conclusions.

working hypothesis is that blue and red clusters have very similar profiles and both approximate well the galaxy light.

5. A spherical galaxy model

5.1. The brightness profile

We employed the IRAF tasks *ellipse* and *bmodel* for investigating the brightness profile of NGC 7796. The innermost 7″ are saturated in our image. Therefore, we used a short exposure image of NGC 7796, taken with Gemini-South/GMOS as a preimage for a spectroscopic program (GS-2013B-Q-83, :PI: Richtler) to fill the central part This image occupies the GEMINI filter g-G0325 instead of an R-filter, but delivers a brightness profile, which in the overlapping region agrees perfectly with the R-profile from the VIMOS image. It is a safe assumption that within 7″ no significant colour gradient exists, which would prohibit such a procedure.

Since we want to use the surface brightness within a spherical model, we enforce (almost) sphericity in the *ellipse*-task by fixing the ellipticity to 0.05. Objects other than the central galaxy were masked using the "segmentation image" produced by SExtractor (Bertin et al. 1996).

The difficulties, which arise for the profile determination at faint magnitude levels and large radii, have to do with the fact

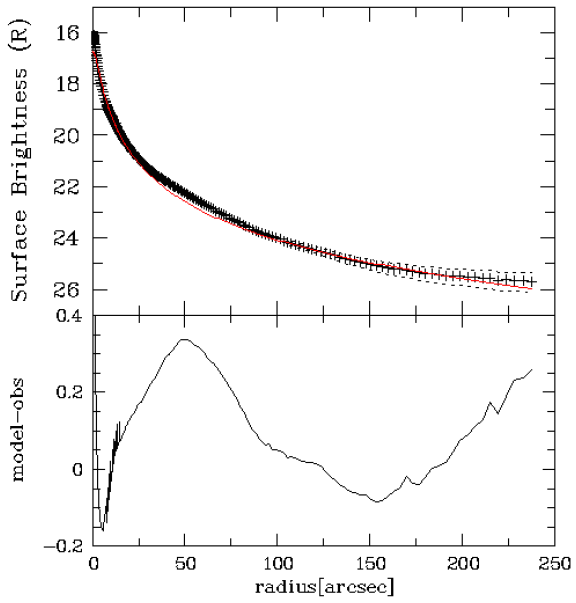

Fig. 8. *Upper panel*: spherical surface brightness profile of NGC 7796 (R-band). The red line is the beta-model (see text), which deviates only within the innermost few arcsec, where the measured profile is more cuspy than the model. The logarithmic derivative assumes the value −2 from approximately 23 arcsec outwards. *Lower panel*: difference model-observations.

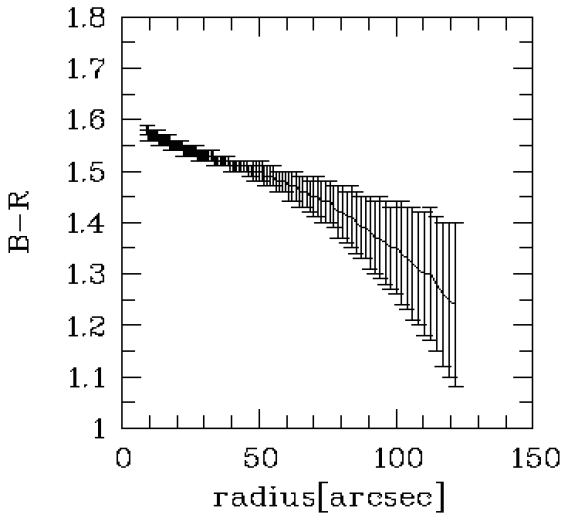

Fig. 9. $B-R$ colour profile for NGC 7796. The uncertainties are given by the *ellipse* task of IRAF.

that the sky is not reached on Q2 itself. Already at a radius of 150″ the isophote touches the frame border and at 250″, the fraction of the isophote covering the frame, is tiny. Therefore, the outermost value of 4625 ADUs cannot be considered to be a valid sky value. From the other quadrants, Q3 deviates significantly. The median value of Q1 is 4548 and of Q4 is 4557, while it is 4138 of Q3. We therefore adopt a value of 4560 as the sky value. An uncertainty of 0.5%, which is perhaps difficult to achieve, corresponds at the outermost data point to ±0.3 mag in the surface brightness.

Applying the calibration relations from Sect. 3.1 results in the following photometric model in the R-band (mag/square arcmin) (see Fig. 8).

$$\mu(R) = -2.5\log\left(a_1\left(1+\left(\frac{R}{R_c}\right)^2\right)^{\alpha}\right) + 8.666 \quad (3)$$

with $a_1 = 5.0\times10^{-4}$, $R_c = 3.4''$, $\alpha = -1.0$.

With the data from Table 1 this model reads in units of $L_\odot/\mathrm{pc}^2$

$$L(R) = 4.28\times10^3\left(1+\left(\frac{R}{R_{\mathrm{pc}}}\right)^2\right)^{\alpha} \quad (4)$$

with $R_{\mathrm{pc}} = 824$ pc, $\alpha = -1.0$.

We used $M_{R,\odot} = 4.42$.

5.2. Colour map and colour profile

We constructed a colour map by applying $-2.5\times\log(B/R)+ZP$, where B, R denote the sky-subtracted images and ZP the zeropoint. No colour term has been applied for the small colour range. The zeropoint has been determined by using the aperture photometry by Poulain (1988) by adopting a colour of $B-R = 1.59$ for the inner region outside the saturated area at a radius of 7″. Except for a rather smooth colour gradient, no structures are visible, which would hint at any recent infall or merger processes. Adopting the models of Marigo et al. (2008), the inner colour fits to a population of 12 Gyr and solar abundance. Figure 9 shows the 1D-colour profile, which has been constructed with *ellipse* from the colour map. The clear bimodality of the GCS colour distribution shows, that intermediate-age GCs do not exist in large numbers. Therefore one concludes that the colour gradient is largely caused by a metallicity gradient and not by intermediate-age stellar populations.

5.3. IMACS data

IMACS data were acquired in the V-band with the idea of looking for large-scale tidal features, indicative of merging processes. Two adjacent, overlapping, pointings were used to produce a field of view of ∼27′ × 40′. Furthermore, short exposure images were obtained to ensure that the central regions, where the VIMOS data is over exposed, can also be analysed.

We removed the galaxy light using the *ellipse* task within IRAF. Subtraction of the galaxy model revealed a paucity of tidal remnants, i.e. the galaxy appears smooth and no tidal features can be seen within these data. The central ∼6 × 6′ of the galaxy-subtracted image can be seen in Fig. 10.

The residuals from the model subtraction in the central region, within ∼45″ of the Galactic centre, show the signature of boxy isophotes (e.g. Jedrzejewski 1987). Note that the tidal tails emanating from the dwarf companion (see Sect. 7) are also obvious in the IMACS data, confirming their reality.

6. Dynamical remarks

The kinematical information available for NGC 7796 is relatively sparse and not always consistent. Moreover, it is restricted to the inner 22″ with only one measurement at 37″. In Fig. 11, we display the velocity dispersions of Bertin et al. (1994, triangles) and Milone et al. (2007, open circles). Beuing et al. (2002) gives a central velocity dispersion of 264 km s^{-1}, which fits very well. At larger radii, the agreement is less good. Bertin et al. give coordinates along a long-slit, which are transformed

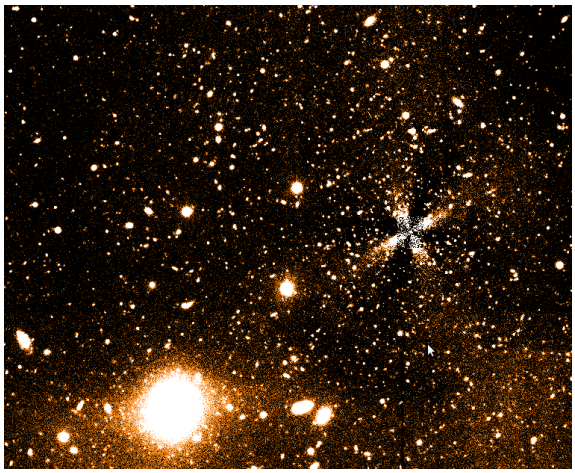

Fig. 10. Part of the IMACS field in the V-band with NGC 7796 subtracted. The central residuals indicate a boxy isophote symmetry, probably reminiscent of dry mergers. The dwarf companion is in the lower left corner. The tidal tails are clearly discernible. The image size is $6' \times 6'$. North is up, east to the left.

in Fig. 11 into absolute radial distances. The scatter may come from the fact that the velocity field of NGC 7796 is not symmetric around the centre, but the outmost point is difficult to reconcile with the inner measurements. However, it has an uncertainty of 50 km s^{-1}. The data of Milone et al. (2007) should have a lower signal-to-noise (S/N; smaller telescope, shorter exposure times), but agree well in the inner region.

We now use our light model from Paper I to investigate by simple dynamical modeling, whether a dark halo is present and what stellar M/L-values are required. We perform spherical Jeans modeling as in previous work. A compilation of the relevant formulae can be found in Mamon & Łokas (2005) and Schuberth et al. (2010) and we refer the reader to these papers for details. In short, we multiply the deprojected light model with an M/L-value and calculate line-of-sight velocity dispersions with certain assumptions concerning the anisotropy. Regarding the anisotropy, we use the results by Hansen & Moore (2006) which suggest a universal relation between the anisotropy parameter β of the Jeans-equation and the logarithmic slope of the density profile of the form $\beta = -0.1 \times -0.2 \times slope(r)$. We deproject our photometric model (see e.g. Schuberth et al. 2010 for the deprojection formula) and get for the luminosity density $j(r)$:

$$j(r) = 2.59 \times \left(1 + \left(\frac{r}{825.4\ \mathrm{pc}}\right)^2\right)^{-1.5} L_\odot/\mathrm{pc}^3. \quad (5)$$

For our $j(r)$ this means a quick rise until $\beta = 0.4$ at about 2 kpc, followed by a smooth increase until $\beta = 0.45$ at 10 kpc. This behaviour can be well approximated by formula (60) of Mamon & Łokas (2005) so that the corresponding formulae for calculating the line-of-sight velocity dispersion can be applied. Formula (60) then becomes $\beta = 0.5 \times r/(r + 500\ \mathrm{pc})$.

Figure 11 shows in its upper panel the isotropic case for "stars only" and the MONDian case (e.g. Milgrom 2012) which has been calculated from the Newtonian circular velocity v_N by

$$v_\mathrm{M} = \sqrt{v_\mathrm{N}^2(r)/2 + \sqrt{v_\mathrm{N}^4(r)/4 + v_\mathrm{N}^2(r)a_0 r}} \quad (6)$$

where v_M is the MONDian circular velocity and $a_0 = 1.3 \times 10^{-8}$ cm/s^2 (see also Richtler et al. 2011). Indicated in the figure are the M/L-values in the R-band, which have been used for

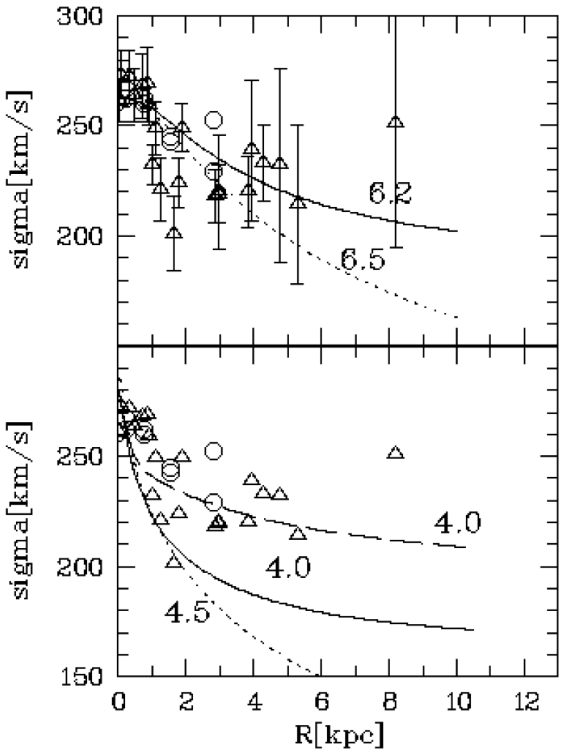

Fig. 11. *Upper panel*: available kinematic data together with isotropic models. The circles are measurements by Milone et al. (2007), the triangles by Bertin et al. (1994). The central velocity dispersion of 264 km s^{-1} by Beuing et al. (2002) is not shown. Error bars are omitted for readability. Plotted are galactocentric distances, irrespective of minor or major axis or intrinsic deviations from central symmetry. The short-dashed line is an isotropic model without dark matter with the stellar M/L_R-value indicated, the solid line is an isotropic MOND model. *Lower panel*: anisotropic models (see text). The solid line is a MONDian model. The long-dashed line is the sum of a stellar contribution with $M/L_R = 4.0$ plus a logarithmic dark halo. The anisotropy cannot be very strong in which case a MONDian halo might be a good description.

these models. The requirement was to reproduce the measurements by Milone et al. (2007) which here appear in our spherical model as the mean values of the minor and major axes. The outer value of Bertin et al. (1994) cannot be reproduced within our model with any reasonable halo.

In the isotropic case, a stellar M/L_R of about 6.5 is necessary to reproduce the inner velocity dispersions. This fits well to the analysis of the stellar population by Milone et al. (2007), who found the central population metal-rich and very old. The SSP-models of Marigo et al. (2008) give $M/L_R = 6.0$ for an age of 11 Gyr, a metallicity $z = 0.04$, and a log-normal Chabrier-IMF. Adopting a Kroupa-IMF results in $M/L_R = 7.7$. Given the uncertainty in the distance and the fact that M/L-values are inversely proportional to the assumed distance, the model values are in reasonable agreement and the need for additional dark matter cannot be concluded. However, these M/L-values are *global* M/L-values. As the colour gradient of the galaxy light shows, this global values must be lower than the central M/L-values. We need to measure the population properties at larger radii before better models can be delevoped.

Assuming MOND (solid line), the M/L-values do not change much. In our model, the MONDian ghost-halo (a spherical Newtonian halo, which is added to the stellar mass and has the MONDian circular velocities) corresponds to a mass of about $6 \times 10^{10}\ M_\odot$ within 10 kpc.

The radially anisotropic case faces some difficulties. As the lower panel of Fig. 11 shows, dark matter is clearly needed to match all measured velocity dispersions. But since a radial anisotropy boosts the central dispersion values, lower stellar M/L-values are required. If dark matter is added, these values must be even lower and cause a contradiction to the population analysis in the centre. This is illustrated by showing a logarithmic halo (long-dashed line), whose circular velocities are

$$v_{\rm circ}(r) = \frac{v_0 r}{\sqrt{r_0^2 + r^2}}. \quad (7)$$

In the present case, $v_0 = 350$ km s^{-1} and $r_0 = 2.5$ kpc, while $M/L_R = 4.0$, which is incompatible with the age of the central stellar population. Whether it is compatible with the global M/L, remains to be investigated. Moreover, the halo has a central density of about 1.1 $M_\odot$/pc^3. Such a high dark matter density is unprobable (Tortora et al. 2009; Napolitano et al. 2010). We conclude that at best mild radial anisotropies are consistent with the measured velocity dispersion within our spherical model. More remarks in Sect. 8.4.

The solid line is a MONDian model with $M/L_R = 4.0$. Increasing this value to match the observations would result in a too high velocity dispersion in the centre. Therefore, a MONDian behaviour of NGC 7796 seems to be possible in case of a weak radial anisotropy, but better kinematical data are required for such an analysis.

7. The companion galaxy APMUKS(BJ) B235639.76-554544.9

There are some galaxies, presumably dwarf galaxies, around NGC 7796, but the radial velocities of these objects are unknown. The only galaxy, where a connection with NGC 7796 is obvious, is a dwarf galaxy 2.6′ to the south-east. It appears in the list of Vader & Chaboyer (1994) as NGC 7796-1 (the NED identification is given in the section title). Vader & Chaboyer (1994) give general photometric properties, classify it as a non-nucleated dwarf, but mention a light excess. The properties which makes this object particularly interesting, are: the tidal tail, the multiple nuclei, the changing of ellipticity and position angle, and the very boxy inner isophotes, which may indicate a previous merger (Khochfar & Burkert 2005). These features are visible in Figs. 12 and 13.

The left panel of Fig. 13 shows the inner area of 30″ × 30″, where three sources are visible. For better readability, we identify them on the right panel with A, B, and C. Source A is the brightest and most compact. It gives the impression of the generic nucleus, while the other sources are more diffuse. The projected distance between A and B is about 590 pc. The right panel is a colour map of the same region. Outside the central sources, the colour is $B - R = 1.25$, but for the sources A, B and C, the bluest colours are $B - R = 0.92$, $B - R = 0.75$, $B - R = 0.95$, respectively. These objects also appear as slightly extended sources in the photometric catalogue. Table 4 lists their magnitudes and colours as they appear in our photometric catalogue. They may be approximate due to the extreme crowding and the extended nature of the sources.

The metallicity is unknown, however, assuming [Fe/H] ≈ −0.5, as is typical of a dwarf galaxy of this brightness, the SSP models by Marigo et al. (2008) provide the ages and masses (via M/L-values) presented in Table 4.

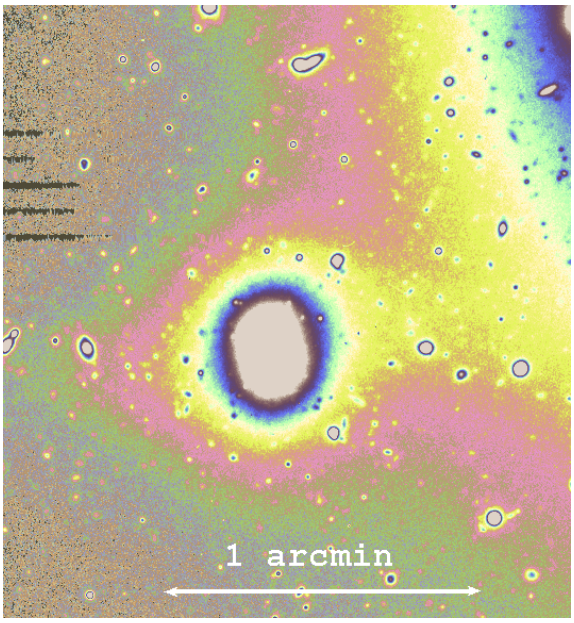

Fig. 12. Companion of NGC 7796 (display: skycat, random6, log). One sees the tidal tails, the isophote twists, and the inner very boxy isophotes. North is up, east to the left.

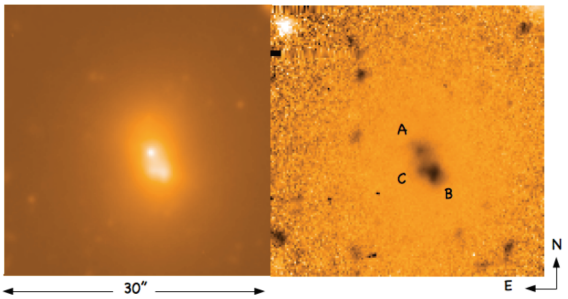

Fig. 13. *Left panel*: central region of the dwarf companion with the multiple nuclei. The side length is 6.55 kpc. *Right panel*: colour map where dark corresponds to bluer colours and bright corresponds to redder colours. See text for more details.

Table 4. Properties of NGC 7796-1 and its nuclei.

Object	R	$B-R$	M_R	Age[×10^9 yr]	Mass[×10^6 $M_\odot$]
NGC 7796-1	15.68	1.25	−17.8	2.7	930
A	21.1	1.06	−12.4	1.7	4.6
B	21.3	0.65	−12.2	0.96	2.8
C	21.5	0.83	−12.0	1.4	2.8

Notes. Ages and masses are derived from SSP models according to Marigo et al. (2008) assuming [Fe/H] = −0.5. The R-magnitude of NGC 7796-1 derives from the B-mag of Vader & Chaboyer (1994) and our $B-R$ colour.

We derive the light profile from an elliptical model of the galaxy. Before running the *ellipse*-task, we subtracted all point sources around NGC 7796-1 and masked the remaining extended sources (not the central sources). The isophote centre was fixed 1.4″ from source A on the line connecting A and B. We applied *ellipse* varying the position angle and the ellipticity. Figure 14 shows the results. For radii larger than 15″ , the surface brightness profile (upper left) is influenced by the light from

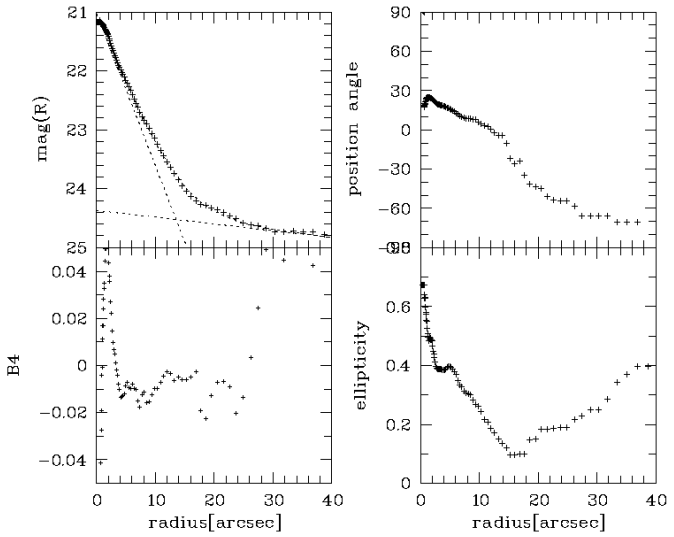

Fig. 14. *Upper left*: surface brightness profile of NGC 7796-1, as measured by *ellipse*, if the position angle is allowed to vary. The two short-dashed lines indicate the two components of the exponential profiles. *Lower left*: the fourth harmonic cosine-term (B4) as defined by *ellipse*. Negative values indicate boxy isophotes. *Upper right*: position angle of the major axis. From north to east: positive, from north to west: negative. Note that isophotes have position angles similar to the axis connecting the nuclei A and B. At larger radii, the isophotes are determined by the tidal tails and the light of NGC 7796. *Lower right*: ellipticity. The variation at larger radii is due to the tidal tail and the neighbouring NGC 7796.

NGC 7796 and from the tidal tails. A good representation of the light profile n the R-band is the sum of two exponentials:

$$\mu(R) = -2.5 * \log((10^{(-0.4*21.014)} \times \exp(-R/4.19)) + 10^{(-0.4*24.368)} \times \exp(-R/94.5)) \quad (8)$$

where R is in arcsec. The outer profile (see Fig. 14) is determined by the tidal tails. The effective radii are for the two components $R_{\rm eff}$ = 7.01″ (=1.7 kpc, inner) and $R_{\rm eff}$ = 158.6″ (=38.45 kpc, outer). The total effective radius is 32″ (=3.05 kpc).

The inner part of the profile is also well described by a Sersic profile with an effective radius of 10.68″ (=2.59 kpc)

$$\mu(r) = 23.271 + (2.1705 * 1.203 - 0.3551) * ((R/10.683)^{(1/1.203)} - 1). \quad (9)$$

In nearby galaxy clusters, the early-type dwarf galaxies show a surprisingly constant effective radius, independent of brightness, of about 950 pc (Smith Castelli et al. 2008; Misgeld et al. 2008). Figure 6 of Misgeld & Hilker (2011) shows that NGC 7796-1 would be located at the upper limit of the distribution and its large $R_{\rm eff}$ might well be caused by a former merging process.

The shifts of the position angle (upper right) and the ellipticity (lower right) are like the outer profile not intrinsic properties of NGC 7796-1.

The ellipticity passes through a minimum, because the direction towards the tidal tails and NGC 7796 almost coincides with the inner minor axis. Thus with increasing radius, the brightness along the inner minor axis declines slower than that along the major axis, until the isophotes become circular and the outer major axis develops. It is an interesting observations that the position angle of the connection of the nuclei A and B, which is 33°,

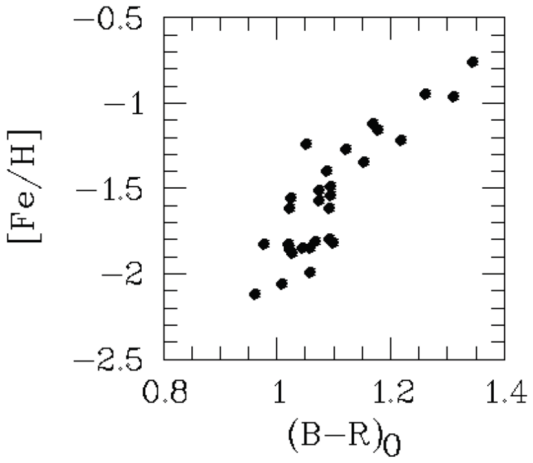

Fig. 15. Integral $B-R$ colours of Galactic GCs with reddenings $E(B-V)$ less than 0.15 versus metallicities. Data are from Harris (1996, 2010 edition). Colour is no longer a reliable indicator for metallicities less than about [Fe/H] = −1.3. This is the main reason for the existence of a "blue peak".

is quite similar to the isophote ellipticity also at larger radii, where the sources themselves do not influence the isophote. Or in other words: the sources know about the shape on the larger scale, which might support the scenario that both are nuclei of the pre-merger components.

8. Discussion

In the following, we comment on some particularly interesting topics and properties of NGC 7796 and its cluster system.

8.1. Bimodality

The bimodal colour structure as in Fig. 5, which is already visible in Fig. 4, although well known in GCSs for many years, has again become a topic of intense discussion recently (for a recent review, see e.g. Richtler 2013). The question was, whether a bimodal colour distribution also means a bimodal metallicity distribution (Richtler 2006; Yoon et al. 2006; Chies-Santos et al. 2012). However, the main difficulty in connecting the colour distribution of GCs with formation scenarios is the fact that for metal-poor clusters, some colours, in our case $B-R$, becomes largely insensitive for metallicity. Varying the horizontal-branch morphology at a given metallicity strongly influences the integral colour (e.g. Chies-Santos et al. 2012) and the non-linear relation of colour and metallicity depends on the photometric bands (Blakeslee et al. 2012).

The only objects for which we have reliable metallicities and integral colours, are Galactic GCs. As an argumentation aid, we plot the integral $B-R$-colours for Galactic GCs with $E(B-V)$-values less than 0.15, adopted from Harris (1996)(2010 edition). One reads from Fig. 15 that for metallicities less than [Fe/H] = −1.3 and for colours bluer than $B-R$ = 1.2, the relation between colour and metallicity practically ceases to exist. This is the reason for the "blue peak": a large metallicity interval is projected into a narrow colour interval. We have no possibility to reconstruct the metallicity distribution within the mentioned interval from broad band colours alone. The red peak, on the other hand, consists of GCs which have been formed together with the metal-rich bulk population of the galaxy. Thus

this type of bimodality is found generally in giant ellipticals, even if the metallicity distribution may be not bimodal. However, Usher et al. (2012) present metallicities, based on the Calcium triplet for a large sample of clusters in 11 early-type galaxies and generally found a bimodal metallicity distribution.

Having said this, the apparent "blue tilt", as might be present here, hardly indicates a strict magnitude-metallicity relation, unless the population structure of these clusters is a strict function of metallicity, different from the situation in the Milky Way. On the other hand, massive star clusters need massive molecular clouds to form, most probably by the merging of star cluster complexes. This has been convincingly argued in the case of W3, the most massive cluster known (Fellhauer & Kroupa 2005). Another very illustrative example, how massive star clusters form, is the young GC in NGC 6946 described by Larsen et al. (2001). A cluster of about $5-8\times10^5\ M_\odot$ is surrounded by a plethora of less massive clusters in a presumably disk-like configuration where also dust is present. These complexes exist in starburst galaxies or at least in galaxies with a high star formation rate and metal-poor environments are probably forbidden. Moreover, the accretion of dwarf galaxies is partly responsible for the richness of GCSs of galaxies (see Richtler 2013, for a review). It is thus plausible that the most massive clusters have been donated on the average by the most massive galaxies, which have enhanced metallicities.

8.2. Colour profile, population synthesis, chemical evolution

Whether age and/or metallicity is responsible for the observed colour gradient, cannot be known from broad-band photometry. However, in old ellipticals metallicity is supposed to affect the colour more strongly than age. A recent survey of 33 elliptical galaxies (Greene et al. 2013) reveals that at 2 $R_{\rm eff}$, the population is typically metal-poor, old, and has an enhanced alpha-to-iron abundance, which is most easily explained by enrichment from SNII. Whether this applies also to IEs, is not known.

The population synthesis for NGC 7796 of Milone et al. (2007), where 7 populations are involved, results in a quite different mix of age and metallicity. These authors adopt three old populations (G1, G2, G3) with ages between 10−15 Gyr and metallicities between solar and −1.1 dex. Moreover, four young populations (Y1, Y2, Y3, RHII) with ages between 0.01−0.08 Gyr and metallicities between −0.2 and −0.5 dex. Even within their quite restricted radial range, Milone et al. see gradients in the global metallicity and in the alpha elements-to-iron ratio, in the sense that the centre is alpha-overabundant ([Fe/H] ≈ 0.4) and declines to the solar value at their outermost point along the major axis, at about 13″. There the old populations make up 80% of the flux at 5870 Å, while 20% is provided by the young populations.

This is not easily brought into agreement with our colour profile. Let us assume for simplicity only two populations, a 13 Gyr old population with [Fe/H] = 0 dex and a 0.025 Gyr population with [Fe/H] = −0.4 dex. The model colours are $B-R=1.67$ and $B-R=0$, respectively. To reproduce the observed colour at about 10″ of $B-R=1.57$, the young population can only contribute with 2% in the R-band. More knowledge will come from new deep and wide-field spectroscopy.

8.3. Companion

Also in other "isolated" ellipticals, we find dwarf companions with tidal tails (Lane et al. 2013). This fact indicates that this is not a rare event. These dwarf galaxies may be "late stragglers" from an initially much larger population which formed, in large part, NGC 7796. If only the central parts are enriched by SNII, the outer parts by SNIa, which start to become active after about 2 Gyr, one can imagine a scenario in which a group of intermediate-mass gas-rich galaxies have fallen in at early times and became enriched by the intermediate-age stellar population already present. Because the metal-poor part of the GC population is not more extended than the galaxy light itself, these infalling galaxies can not have been very rich in GCs themselves.

A recent paper described the first example of a merging of dwarf galaxies around Andromeda (Amorisco et al. 2014) as a demonstration of the hierarchical structure of the merging process. Simulations of dwarf-dwarf mergers have recently been presented by Cloet-Osselaer et al. (2014) and Deason et al. (2014).

We do not know for certain whether NGC 7796-1 is a merger product, but its properties are very suggestive of this. In particular, its large effective radius might indicate the case (i) of Cloet-Osselaer et al. (2014), where a massive progenitor grows with only a few infalling satellites. Future spectroscopic work will lend more clarity. If so, NGC 7796 provides an even more convincing example than Amorisco et al. (2014) of the scale-free character of this process. Regarding brightness and the blue nucleus, NGC 7796-1 shows some similarity to NGC 205 with its blue nucleus and recent star formation (Monaco et al. 2009).

8.4. Comparison with the X-ray mass, agreements and disagreements

The dynamical mass, based on X-ray-observations with Chandra, has been evaluated by O'Sullivan et al. (2007), who describe the X-ray luminosity profile as a beta-profile. Using their β-value, the scale-radius r_c, and the assumption of a constant temperature, the mass is (Grego et al. 2001)

$$M(r) = \frac{3\beta k T_e}{G\mu m_{\rm p}} \frac{r^3}{r_c^2 + r^2} \tag{10}$$

where G is the constant of gravitation, μ the molecular weight, and $m_{\rm p}$ the proton mass. Within 5 $R_{\rm eff}$ (O'Sullivan et al. 2007, adopt $R_{\rm eff}=25.2''$), they find an M/L_B-value of 10.6, compatible with an old, metal-rich stellar population without the need for a massive dark halo. For example, Marigo et al. (2008) gives $M/L_B=11.0$ for $z=0.04$ and an age of 11.2 Gyr. The corresponding mass is $4.42\times10^{11}\,M_\odot$. At small radii, they find the resulting M/L ratio to be smaller than permitted by the stellar population. O'Sullivan et al. mention the possibilities that the X-ray gas may not be in hydrostatic equilibrium, but in a Galactic wind state, or that the dark halo has such a large core that the increase in M/L becomes apparent only at larger radii.

Applying the above formula with $kT_e=0.53$ keV, $\beta=0.39$, $r_c=0.35''$, and $\mu=0.6$, we get, at a radius of 126″ or 30.54 kpc, a mass of $6.8\times10^{11}\ M_\odot$ and a (deprojected) R-luminosity of $6.05\times10^{10}\ L_{R,\odot}$, which means $M/L_R=11.2$ and about 50% of dark matter. The difference to the values of O'Sullivan et al. probably has its origin in the brightness of NGC 7796, because our X-ray masses agree well with their Fig. 5. Moreover, we cannot confirm that the inner M/L-values are lower than permitted by stellar population properties. For example, within 10 kpc, we find $M/L_R=5.6$.

One may also compare the X-ray mass and luminosity with the relation quoted by Kim & Fabbiano (2013): $L_{\rm X}/10^{40}$ erg/s = $M_{\rm tot}/3\times10^{11}$, where $M_{\rm tot}$ is the total mass within 5 effective

radii and L_X the X-ray luminosity in the band 0.3–8 keV. Five effective radii are 38.54 kpc and the total mass according to Eq. (10) within this radius is 1.1×10^{12} $M_\odot$, where we would expect 2.2×10^{12} $M_\odot$ adopting a luminosity of 7.24×10^{40} erg/s from O'Sullivan et al. (2007).

The MONDian mass with a stellar $M/L_R = 6.2$ at 38.54 kpc is 9.8×10^{11} $M_\odot$, which is in quite good agreement with the X-ray based mass. This M/L-value is quite high, but will lower with any radial anisotropy. Another independent value comes from Magorrian & Ballantyne (2001), who modelled the kinematic data of Bertin et al. (1994) and give a circular velocity of 371 km s^{-1} at 37″. The MONDian model predicts 377 km s^{-1} at this radius.

One can conclude on the basis of X-rays that NGC 7796 is a promising candidate for an isolated galaxy with a MONDian behaviour. The available kinematical data are not yet precise enough to make stronger statements. We remind the case of NGC 7507, which in the sample of Kronawitter et al. (2000) was one of the most dark matter dominated galaxies and lost this status completely in the investigation of Salinas et al. (2012).

On the other hand, Milgrom (2012) found good agreement with the MONDian predictions for the isolated ellipticals NGC 1521 and NGC 720. Memola et al. (2011) investigated NGC 7052 and NGC 7785 and found disagreement with MOND. This issue is still open and NGC 7796 might become an important cornerstone in this respect, once a thorough stellar dynamical investigation reaching large radii, becomes available.

9. Summary and conclusions

We investigated the globular cluster system of the isolated elliptical galaxy NGC 7796 on the basis of imaging in B and R with VLT/VIMOS. Moreover, we measured the galaxy's light profile and provided possible dynamical models based on kinematical data from the literature. Additionally, we investigated the structure and morphology of the neighbouring dwarf galaxy NGC 7796-1.

Our main findings/conclusions are the following:

- The GCS has about 2000 members, and is relatively rich in comparison to other isolated ellipticals. The specific frequency is about 2.5 ± 0.6.
- The colour distribution of clusters resembles that of old giant ellipticals in galaxy clusters showing a clear bimodality, whose origin is mainly the non-linear relation between colour and metallicity. The colour distribution spans quite precisely the entire metallicity range, which is expected for old globular clusters. No indication of a younger population of globular clusters has been found.
- No structural abnormalities such as shells or ripples, common among isolated ellipticals, have been found. This matches the understanding of NGC 7796 as an old galaxy, where signs of merging or tidal interactions have already disappeared.
- A very massive dark halo seems to be excluded. The central velocity dispersion can be reproduced by the normal M/L-value for an old, metal-rich population. However, some dark matter, for instance as required for the baryonic Tully-Fisher relation, might be present. The available kinematical data do not permit strong conclusions regarding MOND, but the X-ray data support it as well as does earlier dynamical modelling. More certainty must be left for future work which will measure the entire velocity field and the kinematic properties at larger radii.
- The companion of NGC 7796 shows tidal tails, demonstrating its interaction with NGC 7796. It also presents multiple nuclei and boxy isophotes, suggestive of a merger.

NGC 7796 appears to be a genuine elliptical galaxy. That isolated elliptical galaxies, as listed in catalogues, do not belong to a class with common class properties can be seen from different angles. The X-ray properties of the Memola et al. (2009) sample cover a broad range of luminosities. There are old galaxies like NGC 7796, but also galaxies with more recent star formation events and galaxies with morphological peculiarities that are indicative of galaxy interactions. The investigation of the dark matter properties of isolated ellipticals is still at its beginning. There is support for MOND, but also some tension there, as well as tension with the usual CDM scenario. Stellar dynamical tracers at large radii are needed for deeper insights.

Acknowledgements. T.R. acknowledges FONDECYT project Nr. 1100620 and the BASAL Centro de Astrofísica y Tecnologías Afines (CATA) PFB-06/2007. He also acknowledges gratefully a visitorship at ESO/Garching, where this paper has been completed. R.R.L. gratefully acknowledges financial support from FONDECYT, project No. 3130403. This research has made use of the NASA/IPAC Extragalactic Database (NED) which is operated by the Jet Propulsion Laboratory, California Institute of Technology, under contract with the National Aeronautics and Space Administration.

References

Amorisco, N. C., Evans, N. W., & van de Ven, G. 2014, Nature, 507, 335
Bertin, G., Bertola, F., Buson, L. M., et al. 1994, A&A, 292, 381
Bettoni, D., Galletta, G., & Prada, F. 2001, A&A, 374, 83
Beuing, J., Bender, R., Mendes de Oliveira, C., Thomas, D., & Maraston, C. 2002, A&A, 395, 431
Blakeslee, J. P., Cho, H., Peng, E. W., et al. 2012, ApJ, 746, 88
Buote, D. A., Jeltema, T. E., Canizares, C. R., & Garmire, G. P. 2002, ApJ, 577, 183
Caso, J. P., Richtler, T., Bassino, L. P., et al. 2013, A&A, 555, A56
Chies-Santos, A. L., Larsen, S. S., Cantiello, M., et al. 2012, A&A, 539, A54
Cho, J., Sharples, R. M., Blakeslee, J. P., et al. 2012, MNRAS, 422, 3591
Cloet-Osselaer, A., De Rijcke, S., Vandenbroucke, B., et al. 2014, MNRAS, 442, 2909
Collobert, M., Sarzi, M., Davies, R. L., Kuntschner, H., & Colless, M. 2006, MNRAS, 370, 1213
Deason, A., Wetzel, A., & Garrison-Kimmel, S. 2014, ApJ, 794, 115
Dirsch, B., Richtler, T., Geisler, D., et al. 2003, AJ, 125, 1908
Erben, T., Schirmer, M., Dietrich, J. P., et al. 2005, Astron. Nachr., 326, 432
Fellhauer, M., & Kroupa, P. 2005, MNRAS, 359, 223
Greene, J. E., Murphy, J. D., Graves, G. J., et al. 2013, ApJ, 776, 64
Grego, L., Carlstrom, J. E., Reese, E. D., et al. 2001, ApJ, 552, 2
Hansen, S. H., & Moore, B. 2006, New Astron., 11, 333
Harris, W. E. 1996, AJ, 112, 1487
Hau, G. K. T., & Forbes, D. A. 2006, MNRAS, 371, 633
Hernández-Toledo, H. M., Vázquez-Mata, J. A., Martínez-Vázquez, L. A., et al. 2008, AJ, 136, 2115
Jedrzejewski, R. I. 1987, MNRAS, 226, 747
Karachentseva, V. E. 1973, Astrofizicheskie Issledovaniia Izvestiya Spetsial'noj Astrofizicheskoj Observatorii, 8, 3
Karachentseva, V. E., Lebedev, V. S., & Shcherbanovskij, A. L. 1997, VizieR Online Data Catalog, VII/82A
Kauffmann, G. 1996, MNRAS, 281, 487
Khochfar, S., & Burkert, A. 2005, MNRAS, 359, 1379
Kim, D.-W., & Fabbiano, G. 2013, ApJ, 776, 116
Kronawitter, A., Saglia, R. P., Gerhard, O., & Bender, R. 2000, A&AS, 144, 53
Kuntschner, H., Smith, R. J., Colless, M., et al. 2002, MNRAS, 337, 172
Landolt, A. U. 1992, AJ, 104, 340
Lane, R. R., Salinas, R., & Richtler, T. 2013, A&A, 549, A148
Larsen, S. S., Brodie, J. P., Huchra, J. P., Forbes, D. A., & Grillmair, C. J. 2001, AJ, 121, 2974
Magorrian, J., & Ballantyne, D. 2001, MNRAS, 322, 702
Mamon, G. A., & Łokas, E. L. 2005, MNRAS, 363, 705
Marcum, P. M., Aars, C. E., & Fanelli, M. N. 2004, AJ, 127, 3213
Marigo, P., Girardi, L., Bressan, A., et al. 2008, A&A, 482, 883
Memola, E., Trinchieri, G., Wolter, A., Focardi, P., & Kelm, B. 2009, A&A, 497, 359

Memola, E., Salucci, P., & Babić, A. 2011, A&A, 534, A50
Méndez, R. H., Teodorescu, A. M., Kudritzki, R.-P., & Burkert, A. 2009, ApJ, 691, 228
Milgrom, M. 2012, Phys. Rev. Lett., 109, 131101
Milone, A. D. C., Rickes, M. G., & Pastoriza, M. G. 2007, A&A, 469, 89
Misgeld, I., & Hilker, M. 2011, MNRAS, 414, 3699
Misgeld, I., Mieske, S., & Hilker, M. 2008, A&A, 486, 697
Monaco, L., Saviane, I., Perina, S., et al. 2009, A&A, 502, L9
Mulchaey, J. S., & Zabludoff, A. I. 1999, ApJ, 514, 133
Napolitano, N. R., Romanowsky, A. J., & Tortora, C. 2010, MNRAS, 405, 2351
Niemi, S.-M., Heinämäki, P., Nurmi, P., & Saar, E. 2010, MNRAS, 405, 477
O'Sullivan, E., Sanderson, A. J. R., & Ponman, T. J. 2007, MNRAS, 380, 1409
Poulain, P. 1988, A&AS, 72, 215
Prugniel, P., & Heraudeau, P. 1998, A&AS, 128, 299
Reda, F. M., Forbes, D. A., Beasley, M. A., O'Sullivan, E. J., & Goudfrooij, P. 2004, MNRAS, 354, 851
Rejkuba, M. 2012, Ap&SS, 341, 195
Richtler, T. 2003, in Stellar Candles for the Extragalactic Distance Scale (Berlin Springer Verlag), eds. D. Alloin, & W. Gieren, Lect. Notes Phys., 635, 281
Richtler, T. 2006, BASI, 34, 83
Richtler, T. 2013, in 370 Years of Astronomy in Utrecht, eds. G. Pugliese, A. de Koter, & M. Wijburg, ASP Conf. Ser., 470, 327
Richtler, T., Famaey, B., Gentile, G., & Schuberth, Y. 2011, A&A, 531, A100
Salinas, R., Richtler, T., Bassino, L. P., Romanowsky, A. J., & Schuberth, Y. 2012, A&A, 538, A87
Schirmer, M. 2013, ApJS, 209, 21
Schlegel, D. J., Finkbeiner, D. P., & Davis, M. 1998, ApJ, 500, 525
Schuberth, Y., Richtler, T., Hilker, M., et al. 2010, A&A, 513, A52
Smith, R. M., Martínez, V. J., & Graham, M. J. 2004, ApJ, 617, 1017
Smith Castelli, A. V., Bassino, L. P., Richtler, T., et al. 2008, MNRAS, 386, 2311
Spitler, L. R., Forbes, D. A., Strader, J., Brodie, J. P., & Gallagher, J. S. 2008, MNRAS, 385, 361
Tal, T., van Dokkum, P. G., Nelan, J., & Bezanson, R. 2009, AJ, 138, 1417
Thomas, D., Maraston, C., Bender, R., & Mendes de Oliveira, C. 2005, ApJ, 621, 673
Tonry, J. L., Dressler, A., Blakeslee, J. P., et al. 2001, ApJ, 546, 681
Tortora, C., Napolitano, N. R., Romanowsky, A. J., Capaccioli, M., & Covone, G. 2009, MNRAS, 396, 1132
Turner, E. L., & Gott, III, J. R. 1976, ApJS, 32, 409
Usher, C., Forbes, D. A., Brodie, J. P., et al. 2012, MNRAS, 426, 1475
Vader, J. P., & Chaboyer, B. 1994, AJ, 108, 1209
van Dokkum, P. G., Whitaker, K. E., Brammer, G., et al. 2010, ApJ, 709, 1018
Villegas, D., Jordán, A., Peng, E. W., et al. 2010, ApJ, 717, 603
Yoon, S.-J., Yi, S. K., & Lee, Y.-W. 2006, Science, 311, 1129